

# Asteroid Radar Astronomy

**Steven J. Ostro**

*Jet Propulsion Laboratory, California Institute of Technology*

**R. Scott Hudson**

*Washington State University*

**Lance A. M. Benner and Jon D. Giorgini**

*Jet Propulsion Laboratory, California Institute of Technology*

**Christopher Magri**

*University of Maine at Farmington*

**Jean-Luc Margot**

*California Institute of Technology*

**Michael C. Nolan**

*Arecibo Observatory*

---

Radar is a uniquely powerful source of information about the physical properties and orbits of asteroids. Measurements of the distribution of echo power in time delay (range) and Doppler frequency (radial velocity) produce two-dimensional images that can provide spatial resolution as fine as a decameter if the echoes are strong enough. With adequate orientational coverage, such images can be used to construct detailed three-dimensional models, define the rotation state precisely, and constrain the object's internal density distribution. As of May 2002, radar signatures have been measured for 75 main-belt asteroids (MBAs) and 105 near-Earth asteroids (NEAs). We summarize specific results for radar-detected asteroids, which span 4 orders of magnitude in diameter and rotation period. Radar has revealed both stony and metallic objects, principal-axis and complex rotators, smooth and extremely rough surfaces, objects that must be monolithic and objects that probably are not, spheroids and highly elongated shapes, contact-binary shapes, and binary systems. Radar also has expanded accurate orbit-prediction intervals for NEAs by as much as several centuries.

## 1. INTRODUCTION

One of the goals of this book is to outline developments since *Asteroids II* (Binzel *et al.*, 1989), which was completed in 1988. The subsequent 13 years have seen critical developments in technical aspects of asteroid radar astronomy, including increases in sensitivity and versatility of telescopes, the evolution and optimization of observational techniques, and the invention of analytical methods to optimize extraction of information from radar images. Observations commensurate with those developments have raised the number of radar-detected asteroids from 52 (19 NEAs + 33 MBAs) in mid-1988 (Ostro, 1989) to 180 (105 NEAs + 75 MBAs) in May 2002 and have produced an enormous body of information about the physical properties of asteroids. An equally significant development since *Asteroids II* is an increase in the number of persons lead-authoring asteroid radar papers at an average rate of one person per year.

The following sections outline the technical developments and observational highlights of the past 13 years,

summarize the major conclusions drawn from the explosive increase in data, and discuss current problems and challenges to be faced during the coming decade. See Ostro (2002a) for a list of radar-detected asteroids, Ostro (1993, 2002b) for reviews of planetary radar principles and techniques, Ostro (1994) for a discussion of radar's role in NEO hazard identification and mitigation, and Harmon *et al.* (1999) for a review of radar observations of comets.

## 2. STRATEGIES, TELESCOPES, AND TECHNICAL DEVELOPMENTS

### 2.1. Telescopes and Observing Strategies

The basic strategy of an asteroid radar experiment is to measure the distribution of echo power in time delay and Doppler frequency, usually in the opposite sense (OC) of circular polarization as transmitted as well as in the same sense (SC) as a function of the object's orientation and plane-of-sky (POS) direction. SC echo would be absent in

mirrorlike backscattering from surface elements for which size and radius of curvature are huge compared to the wavelength, but would become increasingly significant if there is near-surface “roughness” at scales near the wavelength or any kind of multiple scattering. Hence SC/OC is a measure of near-surface structural complexity (see section 3).

The achievable delay/Doppler resolution depends first of all on the echo’s signal-to-noise ratio (SNR), the ratio of echo power to the root-mean-square receiver noise. The SNR depends primarily on the target’s distance  $R_{\text{tar}}$ , diameter  $D_{\text{tar}}$ , and rotation period  $P$ ; the telescope’s effective area  $A$  and transmitter power  $P_{\text{tx}}$ ; and the integration time  $\Delta t$

$$\text{SNR} \sim R_{\text{tar}}^{-4} D_{\text{tar}}^{3/2} A^2 P_{\text{tx}} P^{1/2} \Delta t^{1/2} \quad (1)$$

The integration time needed to achieve any given signal-to-noise ratio for a given target increases as  $R_{\text{tar}}^8 A^{-4}$ . This is why the 305-m Arecibo telescope and the 70-m Goldstone antenna (DSS-14) are almost entirely responsible for the history of asteroid radar, why we try to observe asteroids at their closest approaches to Earth, and why observations of extremely close NEAs are especially lucrative.

A major structural upgrading of the Arecibo telescope and modernization of its computer hardware and software have made it an order of magnitude more sensitive and much more versatile than it was a decade ago. Transmitter upgrades and installation of a quasi-optical transmit/receive switch on DSS-14 have increased its effectiveness for NEA radar astronomy by reducing the switching time from  $\sim 20$  s to  $\sim 1$  s. Arecibo can see almost twice as far as Goldstone, but Goldstone’s greater steerability gives it access to twice as much sky and lets it track objects at least  $3\times$  longer than Arecibo. For very close targets, transmit/receive switching and transmitter on/off cycling has been avoided by transmitting continuously from DSS-14 and receiving continuously with DSS-13, a 34-m antenna 22 km from DSS-14 and connected to it by a fiber-optics cable. The complementarity of Arecibo and Goldstone has been exploited frequently.

Given unlimited echo strength, the delay resolution is limited by the rate at which signals produced by available transmitter amplifier tubes (klystrons) can be modulated, currently about 20 MHz, which corresponds to  $0.05 \mu\text{s}$  (7.5 m of range), compared to  $2 \mu\text{s}$  (300 m) when *Asteroids II* was written. The transmitted signal travels the round-trip distance to the target and the echo is measured using what is effectively an extremely sensitive voltmeter, the output of which is sampled and digitized. The received voltage is optionally divided into time-delay cells, and then a  $T_{\text{coh}}$ -long coherent time series of voltage samples within a given time-delay cell is Fourier-transformed to produce a spectrum of the echo power within that cell with a resolution of  $\Delta f = T_{\text{coh}}^{-1}$ . Because of the intrinsically noiselike nature of the voltage samples (*Jenkins and Watts, 1968*), the SNR of a single-power spectrum will generally be  $< 3$  for even the strongest radar echo. The fractional noise (dominated by thermal noise for weak echoes or by “self-noise” for strong ones) in a sum of  $N$  such “looks” is  $N^{-1/2}$ , so it is

desirable to sum many looks. Even when the echo strength overwhelms the thermal noise of the receiver, one sometimes chooses to increase  $N$  in order to reduce the self-noise, consequently sacrificing frequency resolution. Thus, a delay-Doppler image is intrinsically a time exposure, combining coherent integration in the Fourier analysis with incoherent integration in the sum of independent looks. The optimum  $\Delta f$  for an image with a given tolerable level of noise will depend in part on the echo bandwidth, and hence on the target’s size and spin state (see section 2.3).

At radio frequencies, the phase of the electromagnetic field is maintained all the way to the samplers, so the Fourier analysis and summing of looks can be done in software after the fact, allowing SNR to be traded for frequency resolution in the data reduction rather than during the data acquisition. However, measurement of range information requires coding of the transmitted signal, so the range resolution must be chosen before beginning the experiment.

During an observation, one can remove the Doppler frequency shift  $\nu$  introduced by the radial motion of the target by tuning the frequency of either the transmitter or the receiver according to a Doppler-prediction ephemeris, with the goal of ensuring that the frequency corresponding to echoes from the target’s center of mass (COM) is zero in the coordinate system of the acquired data. The Doppler shift varies as the target moves and as the Earth rotates, and it must be adjusted many times per second. One also uses the prediction ephemerides to slew the time base for sampling the echoes in order to register sequential samples of echoes from any given range cell on the target. In practice, there will always be a nonzero error  $\Delta \nu_{\text{eph}}$  in the Doppler-prediction ephemeris, which is equivalent to a nonzero rate of change in the delay-ephemeris’ error  $\Delta \tau_{\text{eph}}$  and hence in the rate of image smearing in delay

$$d\Delta \tau_{\text{eph}}(t)/dt = -\Delta \nu_{\text{eph}}(t)/F_{\text{tx}} \quad (2)$$

where  $F_{\text{tx}}$  is the transmitter carrier frequency (2380 MHz for Arecibo; originally 8495 MHz for Goldstone but changed to 8510 MHz in September 1991 and then to 8560 MHz in March 1999). Thus a reasonably accurate Doppler ephemeris is a prerequisite for imaging with fine range resolution.

Main-belt asteroids that enter the current radar detectability windows usually have many decades of accumulated optical astrometry, so preresearch pointing uncertainties typically are on the order of 1 arcsec, Doppler uncertainties are small compared to the intrinsic frequency dispersion of the echoes, and delay uncertainties are typically of the same order as the object’s diameter. For MBA experiments to date, echo strength has been the only factor that has limited obtainable delay-Doppler resolution.

For NEAs, the accuracy of the ephemerides is often a major concern, and for newly discovered objects it is critical, because ephemeris accuracy decays away from the interval spanned by astrometric data. Often, unless follow-up optical astrometry is obtained between the date of a discovery announcement and the date when an initial radar observation is

TABLE 1. Residuals for past near-Earth-asteroid recoveries.

Object	Recovery Date	O	R	O/R
1989 PB (4769 Castalia)	May 1990	24"	0.4"	60
1991 AQ	September 1994	57°	0.1°	380
1986 DA (6178)	October 1994	56"	0.9"	60
1991 JX (6489 Golevka)	March 1995	3600"	4.6"	780
1986 JK (14827)	April 2000	114°	0.1°	910

Here O represents the residual (i.e., the observed position minus the predicted position) for an orbit solution incorporating only optical astrometry. R represents the residual for an orbit solution using radar as well as optical. O/R is the ratio of residuals for the two cases.

attempted, the pointing uncertainty will be large compared to the  $\sim 2$ -arcmin widths of the Arecibo and Goldstone radar beams. In practice, to avoid an intolerable sacrifice of sensitivity, pointing should be good to at least 15 arcsec. Once echoes have been detected, even coarse Doppler astrometry is adequate to shrink the orbit uncertainties enough to ensure sufficient pointing accuracy throughout the discovery apparition.

## 2.2. Radar Astrometry

Radar reconnaissance of a new NEA generally proceeds from detection and Doppler-ephemeris refinement using a continuous-wave (cw, or monochromatic) waveform to delay-ephemeris refinement using a time-modulated waveform (generally a binary-phase-coded waveform; J. K. Harmon, in preparation, 2002) with a fairly coarse delay-resolution cell (called a baud), to the finest-baud and finest- $\Delta f$  imaging supported by the echo strength. In optimizing a setup's tradeoffs between time resolution, spatial resolution, and noise level, one must consider the accuracy of the delay-Doppler ephemeris and whatever is known about the target's size and spin state. Since NEA radar windows are short and telescope time is precious and difficult to obtain on short notice, rapid refinement of orbits and ephemerides using radar astrometry is critical. Installation of onsite software at Goldstone and Arecibo has permitted radar detection of several newly found NEAs within 12 h of the discovery announcement (1999 TY2, 2001 AV43, and 2001 FR85, all at Arecibo) and has dramatically sped up the progression from cw detection to high-resolution imaging (only 15 min for 2001 FR85).

Almost all radar astrometry (Giorgini, 2002; see also Ostro et al., 1991a, and Yeomans et al., 1992) reports the time delay and/or Doppler frequency (at a given transmitter frequency) corresponding to echoes from the target's center of mass received at a specific UTC epoch and at a particular telescope reference point; the transmitting telescope's reference point also is specified. For most antennas, the reference point is the intersection of the elevation and azimuth axes.

As an example of radar astrometry, imaging of Toutatis (Ostro et al., 1995a) using transmissions from DSS-14 and reception at DSS-13 yielded estimates of the 8510-MHz

Doppler frequency,  $248335.943 \pm 0.04$  Hz, and time delay,  $26.056497203 \text{ s} \pm 0.23 \mu\text{s}$ , corresponding to echoes from the asteroid's center of mass received at December 6, 1992, 16:40:00 UTC. These points' residuals with respect to the most recent Toutatis orbit are  $-0.098$  Hz and  $0.268 \mu\text{s}$ , so their fractional precision is  $10^{-8}$  for the delay and  $10^{-6}$  for the Doppler.

The fine fractional precision of radar astrometry plus its orthogonality to optical angle measurements make it powerful for refining orbits. A single radar detection secures the orbit well enough to prevent "loss" of a newly discovered asteroid (Yeomans et al., 1987). Table 1 lists residuals at the first post-discovery-apparition recovery of several NEAs, for an orbit using just optical data and also for an orbit using both radar and optical data. Table 2 demonstrates how radar shrinks the sky area that must be searched for a given probability of recovering several NEAs observed only during their discovery apparition.

With radar astrometry, the length of the interval over which an asteroid's orbit can be calculated with a given level of accuracy can be increased by decades or centuries even for multiapparition NEAs. Let us give two examples, defining a "reliable" prediction interval as one that encompasses all those approaches to within 0.1 AU from Earth for which the  $3\sigma$  uncertainty in the date of closest approach is less than 10 d. Then for Toutatis, observed with radar during the last three of its five optically observed apparitions, the optical-only interval is 1353–2262 and the radar + optical interval is 1353–2532; uncertainty associated with the very close Earth approach in 1353 precludes reliable identification of earlier close Earth approaches. For the single-apparition object 2001 CP36, the optical-only interval is 1989–2004 and the radar + optical interval is 1718–2225.

Ephemeris uncertainties are strategically important at every stage of an asteroid radar experiment and normally are calculated whenever new radar or optical astrometry warrants orbit refinement. Thus, every astrometric measurement lets one assess the accuracy of both the observing ephemeris and the uncertainties that had been calculated for it. Similarly, postfit residuals (observations minus the values calculated from the orbit solution) let one assess the accuracy both of the astrometry and the uncertainty quoted for it (Table 3).

TABLE 2. Search areas for future near-Earth-asteroid recoveries.

Object	Most Favorable Earth-based Recovery Date	Data Span (d)	Astrometry			Gap (yr)	$3\sigma$ Search Area (arcsec <sup>2</sup> )		
			Optical	Doppler	Delay		O	R	O/R
			1990 OS	November 2003	13		26	2	0
2000 EH26	July 2005	140	49	4	2	4	25772	675	38
1998 ML14	August 2013	225	234	6	6	15	1.9E7	3.8E5	49
2001 AV43	November 2013	38	42	1	0	12	8.9E7	1.8E6	49
1998 KY26	May 2024	11	207	2	2	26	14568	168	87
1999 TY2	October 2064	5	110	1	0	65	2.3E7	1.0E6	23
2001 FR85	March 2081	7	36	3	1	80	1.6E7	1.7E4	956

Each of these objects was observed optically over a short timespan and also was a radar target of opportunity, resulting in the listed numbers of optical (RA + DEC), Doppler, and delay measurements. On the right, we give the total sky area for the  $3\sigma$  orbit-determination uncertainties mapped onto the sky at the next favorable Earth-based recovery date (which we define as the next time when the apparent visual magnitude exceeds 20 during reasonable sky-brightness conditions) for both an optical-data-only (O) orbit solution and a radar + optical-data (R) orbit solution. The O/R ratio conveys how a handful of radar measurements can reduce sky search areas for an object with minimal optical followup astrometry. Dynamical peculiarities unique to each object, such as the number of planetary close approaches, affect these results. For example, 1999 TY2 is unusual in that its  $23^\circ$  inclination to the ecliptic reduces the effects of in-plane gravitational perturbations, which shrinks mapped uncertainties.

TABLE 3. Radar astrometry residuals.

Antennas		Normalized Doppler Residuals			
TX	RCV	mean	$\sigma$	RMS	N
Arecibo	Arecibo	-0.119	0.4547	0.4679	94
DSS 14	DSS 14	-0.160	0.7915	0.8041	113
DSS 14	DSS 13	-0.455	1.095	1.144	12
Haystack	Haystack	-0.452	0.1552	0.4654	2
DSS 14	Evpatoria	0.1629	0.5998	0.6052	18
Sites combined (Doppler):		0.01415	0.6991	0.6978	239

Antennas		Normalized Delay Residuals			
TX	RCV	mean	$\sigma$	RMS	N
Arecibo	Arecibo	0.00044	0.6919	0.6868	68
DSS 14	DSS 14	-0.2510	0.6949	0.7351	88
DSS 14	DSS 13	-0.4635	2.154	2.127	14
Sites combined (delay):		-0.1679	0.9041	0.9170	170
Doppler/delay combined:		-0.06153	0.7949	0.7963	409

Statistics for normalized Doppler and delay postfit residuals ( $r_i$ , the measurement minus that predicted by a weighted-least-squares estimate of the orbit from all optical and radar astrometry, normalized by the measurement uncertainty assigned by the observer) obtained from 1968 through March 2001. Here  $\text{RMS} = [\Sigma(r_i^2)/N]^{1/2}$  and the standard deviation ( $\sigma$ ) equals  $\{\Sigma[(r_i - \bar{r})^2]/(N - 1)\}^{1/2}$ , with  $N$  the number of observations and  $\bar{r}$  the mean residual. Arecibo has historically produced the lowest-noise, least-biased astrometry, followed by DSS-14 (Goldstone). Most of the DSS-13 (Goldstone) astrometry is from the December 1996 Toutatis campaign. Evpatoria results are from the Golevka experiment in 1995. Haystack results are from observations published of asteroid 1566 Icarus in 1968.

When ephemeris uncertainties become smaller than the intrinsic delay-Doppler dispersion of a target's echoes, the challenge becomes to locate the target's COM in the delay-Doppler image plane. The accuracy of this process rests on how well one knows the target's size and shape. Thus, orbit refinement is tightly coupled to determination of physical properties: Radar measurements that produce new infor-

mation about a target's size, shape, rotation, or surface properties generally have astrometric value, and vice versa.

### 2.3. Radar Estimation of Shapes and Spin States

Interpretation of radar images is complicated by the geometry of the delay-Doppler projection (Fig. 1). Constant-

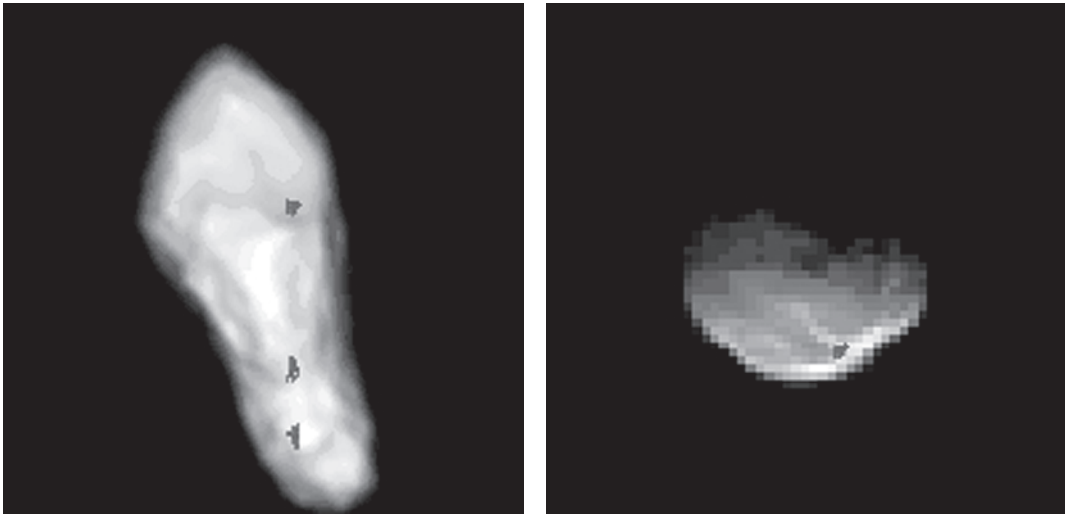


**Fig. 1.** Geometry of delay-Doppler images. The left frame is a plane-of-sky view of the low-resolution radar model of Toutatis (Hudson and Ostro, 1995). Planes of constant time delay (range) are parallel to the plane of the picture. Planes of constant Doppler frequency (line-of-sight velocity) are normal to that plane and aligned vertically. The three dots lie on a line defined by the intersection of a single constant-delay plane and a single constant-Doppler plane. The right frame is a synthesized radar image of the model, arranged so delay increases from bottom to top and Doppler increases from left to right. The three highlighted points on the asteroid model return echo at the single highlighted point in the delay-Doppler image: a three-to-one mapping.

delay planes are normal to the radar line of sight; for a rotating rigid body, constant-Doppler planes are parallel to both the line of sight and the target's apparent spin vector. These two orthogonal sets of parallel planes divide the three-dimensional target into three-dimensional resolution cells in a manner analogous to the way one cuts a potato into strips with rectangular cross sections. In optical imaging, the sets of planes that cut the target are parallel to the line of sight, and we see only the end of each cell that faces us. Thus one knows *a priori* that each point in an optical picture corresponds to a single point on the asteroid's surface — a one-to-one mapping. However, for delay-Doppler imaging, it may be possible for the radar to see both ends of a three-dimensional resolution cell. For very irregular objects, the radar may even see surface elements that lie inside the cell between these ends, e.g., if the cell slices through the sides of a concavity. Thus a delay-Doppler image is generally a many-to-one mapping that contains a form of global aliasing referred to as the north/south ambiguity: One cannot know, *a priori*, which (or even how many) points on the surface contributed echo power to a given pixel.

Moreover, the length equivalent of frequency in an image depends on the asteroid's apparent spin vector  $\mathbf{W}_{\text{app}}$ , as follows: Let us ignore second-order terms (Ostro, 1993, and references therein) and parallax, and assume that the COM is a constant distance from the radar. The Doppler frequency of an echo from a point  $\mathbf{r}$  with respect to the COM is

$$v = (\mathbf{W}_{\text{app}} \times \mathbf{r}) \cdot \mathbf{e} / (\lambda/2) \quad (3)$$

where the unit vector  $\mathbf{e}$  points from the COM to the radar.

The radial velocity equivalent of 1 Hz is half a wavelength ( $\lambda$ ) per second. The target's apparent spin vector satisfies

$$\mathbf{W}_{\text{app}} = \mathbf{W} + \mathbf{W}_{\text{sky}} \quad (4)$$

where  $\mathbf{W}$  is the intrinsic spin vector and  $\mathbf{W}_{\text{sky}}$  is the contribution from the target's apparent plane-of-sky (POS) motion in the frame of the radar telescope. Useful conversion factors are (Ostro et al., 1995a)

$$\begin{aligned} &\text{Goldstone (8560 MHz):} \\ &\text{km/Hz} = 87.2 / |\mathbf{W}_{\text{app}} \times \mathbf{e}| = P / (4.13 \cos \delta) \end{aligned} \quad (5)$$

$$\begin{aligned} &\text{Arecibo (2380 MHz):} \\ &\text{km/Hz} = 312 / |\mathbf{W}_{\text{app}} \times \mathbf{e}| = P / (1.15 \cos \delta) \end{aligned} \quad (6)$$

where  $\mathbf{W}_{\text{app}}$  is in degrees per day,

$$P = 360 / |\mathbf{W}_{\text{app}}| \quad (7)$$

is the instantaneous, apparent spin period in days, and

$$\delta = \cos^{-1}(|\mathbf{W}_{\text{app}} \times \mathbf{e}| / |\mathbf{W}_{\text{app}}|) \quad (8)$$

is the instantaneous, apparent, target-centered declination of the radar.

An asteroid's echo bandwidth is given by

$$B = 4\pi D \cos \delta / \lambda P \quad (9)$$

where  $D$  is the breadth, measured normal to the line of sight,

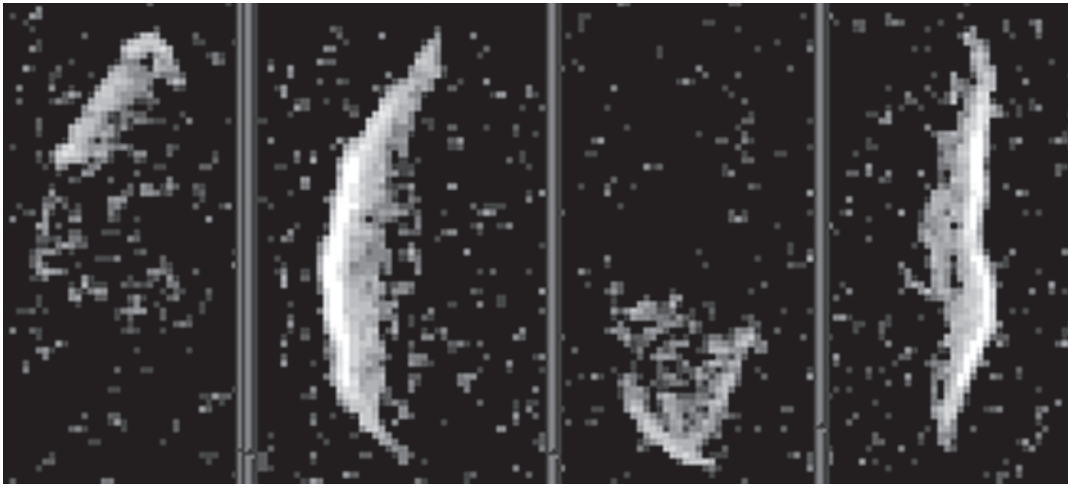


**Fig. 2.** Images of Geographos, taken with the radar close to the asteroid's equatorial plane (*Ostro et al.*, 1996). The four frames were taken with the radar illumination coming from the top, left, bottom, and right. When superposed, the images define the object's pole-on silhouette.

of the asteroid's pole-on silhouette.  $D$  can also be visualized as the asteroid's POS extent normal to the projected apparent spin vector. With  $B$  in Hz, we can write

$$\begin{aligned} &\text{Goldstone (8560 MHz):} \\ &B = 99.7 D \cos\delta / (24 P) \end{aligned} \quad (10)$$

$$\begin{aligned} &\text{Arecibo (2380 MHz):} \\ &B = 27.7 D \cos\delta / (24 P) \end{aligned} \quad (11)$$

For most asteroids,  $\mathbf{W}$  is constant and parallel to both the angular momentum vector  $\mathbf{L}$  and the maximum-moment principal axis of inertia (the asteroid's "short axis"). For such principal-axis (PA) rotators, two constant angles in an inertial frame fix the direction of  $\mathbf{W}$  and the third of these Euler angles gives the rotation phase. However, for a nonprincipal-axis (NPA) rotator (*Hudson and Ostro*, 1995),  $\mathbf{W}$  is not parallel to  $\mathbf{L}$  and is not constant in inertial or body-fixed coordinates. Rather, the body-fixed inertia ellipsoid precesses about  $\mathbf{L}$  while  $\mathbf{W}$  executes a periodic motion in the body, its direction defining a closed curve on the inertia ellipsoid. (All three Euler angles are functions of time.) Given principal moments of inertia  $I_s \geq I_m \geq I_l$  for the short, intermediate and long axes, NPA rotation is defined by eight parameters: two moment-of-inertia ratios, three initial values for the Euler angles, and initial values for each component of  $\mathbf{W}$ . That is, the determinations of spin state and shape are tightly coupled. For a PA rotator, the coupling is loose, and specification of the spin state is trivial. Given Doppler-only images (i.e., cw spectra) that thoroughly sample more than half a rotation, estimates of echo-edge frequencies can be inverted to estimate the shape of the convex hull on a PA rotator's pole-on silhouette (*Ostro et al.*, 1988) as well as the COM echo frequency.

For delay-Doppler images, *Hudson* (1993) showed that a delay-Doppler image sequence can be inverted using constrained least squares to yield estimates of the target's shape,

spin state, and radar-scattering properties, as well as the delay-Doppler trajectory of the COM. This is possible because each surface location has a unique delay-Doppler trajectory as the target rotates, unless the view is equatorial. In that case, the north-south ambiguity cannot be broken, and at best a three-dimensional shape model would convey attributes of the object's shape in a nonunique manner. Ironically, an image sequence taken from within the target's equatorial plane provides unambiguous measurement of the target's pole-on silhouette (Fig. 2; *Ostro et al.*, 1995b, 1996).

The accuracy of radar-based shape reconstruction depends on the echoes' strength and orientational coverage as well as the target's shape and spin state, in a manner that has been calibrated by extensive numerical experiments as well as by laboratory simulations using laser radar and clay models (*Andrews et al.*, 1995). Fortuitously, the Castalia, Toutatis, Geographos, and Golevka imaging experiments during 1989–1996 provided comprehensive experience with nonequatorial and equatorial viewing geometry, with PA and NPA rotators, and with the merits of incorporating optical lightcurves in the inversion (see sections 4.1–4.4).

In inverting radar images, one usually uses a polyhedral shape model with enough vertices to ensure reconstruction of the most detailed structure revealed in the images, while employing penalty functions to suppress structural features not required by the data. A typical approach is to estimate the free parameters  $\mathbf{x}$  by minimizing an objective function

$$\Phi(\mathbf{x}) = \chi^2(\mathbf{x}) + \sum \beta_i \gamma_i(\mathbf{x}) \quad (12)$$

where penalty function  $\gamma_i(\mathbf{x})$  has weight  $\beta_i$  and  $\chi^2(\mathbf{x})$  is the weighted sum of squared residuals between delay-Doppler image pixel values and the corresponding values predicted by the physical model. Penalty functions that may be useful in certain circumstances include dynamical functions that force PA rotation or internal-density homogeneity as well as structural functions that suppress concavities. By exam-

ining how  $\chi^2(\mathbf{x})$  and the distribution of residuals vary as a function of the  $\beta_i$ , one can assess the strength of evidence for such characteristics as complex rotation, nonuniform internal density, shape bifurcation, and exotic topography.

Reconstruction of shapes and spin states of NPA rotators like Toutatis is extremely difficult because of the nature of the coupling between the eight spin-state parameters and the shape parameters. NPA rotations can lead to enhanced orientational coverage, but they also tend to be extremely slow (as expected theoretically; *Harris, 1994*), so many days of radar observations are needed to obtain enough orientational and POS coverage to constrain all the spin parameters.

Asteroids for which radar-based shape constraints have been published are listed in Table 4 in order of decreasing SNR of the data. Of the several asteroids imaged at useful resolutions by spacecraft, Eros (*Veverka et al., 2000*) is the only one for which radar-derived shape constraints are available. Goldstone echo spectra (Doppler-only “one-dimensional images”) were obtained in 1975 by *Jurgens and Goldstein (1976)* with a nearly equatorial view and a total signal-to-noise ratio (SNR) of only  $70\sigma$ . Hence those ancient radar data contain much less useful shape information compared to the other datasets listed in Table 4. *Ostro*

*et al. (1990b)* used spectral-edge frequencies to estimate the hull H on the asteroid’s pole-on silhouette S, and *Mitchell et al. (1998)* applied *Hudson’s (1993)* shape reconstruction methodology to all echo spectral elements ( $\sim 15\times$  more data points) to estimate S. The radar-derived estimates of H (Fig. 3) and S reproduce the object’s pole-on shape characteristics within the associated uncertainty intervals (*Ostro et al., 2000b*), lending confidence to shape reconstructions based on superior datasets.

Accurate shape models of small NEAs open the door to a wide variety of theoretical investigations that are central to understanding the nature, origin, and evolution of these objects but previously have been impossible or have used simplistic models (spheres or ellipsoids). For example, with detailed models of real objects, it is possible to explore the evolution and stability of close orbits (*Scheeres et al., 1996, 1998, 2000*) with direct application to the design of spacecraft rendezvous and landing missions, studies of retention and redistribution of impact ejecta, and questions about the origins and lifetimes of asteroidal satellites. Given information or a realistic assumption about the internal density distribution, one can use a shape model to estimate the distribution of gravitational slopes, which can elucidate characteristics

TABLE 4. Radar shape constraints.

Asteroid	SNR	Delay, Doppler Cells	Max. $ \delta $	Sky Arc	Shape Constraint	Reference
4179 Toutatis	10000	40,50	80°	127°	3D: 1600	<i>Hudson and Ostro (1995)</i>
	10000	160,200	80°	127°	3D: 20000	R. S. Hudson et al. (personal communication, 2001)
6489 Golevka	2000	25,15	66°	94°	3D: 1024, H	<i>Hudson et al. (2000a)</i>
1620 Geographos	2000	68,55	10°	5°	H,S	<i>Ostro et al. (1995b, 1996)</i>
					3D: 512	<i>Hudson and Ostro (1999)</i>
4769 Castalia	1000	4,10	35°	1°	H	<i>Ostro et al. (1990a)</i>
					3D: 167	<i>Hudson and Ostro (1994)</i>
1998 ML14	1000	20,25	50°	33°	3D: 512	<i>Ostro et al. (2001a)</i>
7822 (1991 CS)	800	0,50	?	40°	H	<i>Benner et al. (1999a)</i>
216 Kleopatra	200	15,30	60°	3°	3D: 256	<i>Ostro et al. (2000a)</i>
1862 Apollo	200	12,0	10°	1°	H	<i>Ostro et al. (2002)</i>
1998 KY26	100	1,14	50°	54°	3D: 124	<i>Ostro et al. (1999a)</i>
2063 Bacchus	80	8,6	20°	30°	3D: 256	<i>Benner et al. (1999b)</i>
6178 1986 DA	80	2,20	?	1°	H	<i>Ostro et al. (1991b)</i>
433 Eros	70	0,30	10°	8°	E	<i>Jurgens and Goldstein (1976)</i>
					H	<i>Ostro et al. (1990b)</i>
					3D: 128, S	<i>Mitchell et al. (1998)</i>
2100 Ra-Shalom	70	0,30	?	8°	H	<i>Shepard et al. (2000)</i>
1685 Toro	50	0,11	?	13°	E	<i>Ostro et al. (1983)</i>
					H	<i>Ostro and Connelly (1984)</i>
1620 Ivar	50	5,10	?	7°	H	<i>Ostro et al. (1990c)</i>

Radar-based shape constraints include the pole-on silhouette (S), the hull (H) on that silhouette, triaxial ellipsoid models (E), and three-dimensional shape models (3D: number of shape parameters) reconstructed using *Hudson’s (1993)* technique. Here SNR is the approximate signal-to-noise ratio of an optimally filtered sum of all echoes. The next column gives the maximum number of delay and Doppler resolution cells placed on the target, the maximum asteroid-centered declination  $|\delta|$  achieved during the observations, and the plane-of-sky arc spanned. Existing radar data can support estimation of three-dimensional shape models for 6178 (1986 DA), 7822 (1991 CS), 4197 (1982 TA), 7482 (1994 PC1), 6037 (1988 EG), 1036 Ganymede, 10115 (1992 SK), 1999 JM8, 1999 RQ36, 4486 Mithra, 2100 Ra-Shalom, 2000 RD53, 2000 DP107, 2000 UG11, 4183 Cuno, 2000 YA, 2000 XK47, 2000 YF29, 23187 (2000 PN9), 29075 (1950 DA), 25143 (1998 SF36), 2000 EE104, 1999 KW4, 2000 PH5, 22771 (1999 CU3), 1998 ST27, 33342 (1998 WT24), and 4660 Nereus.

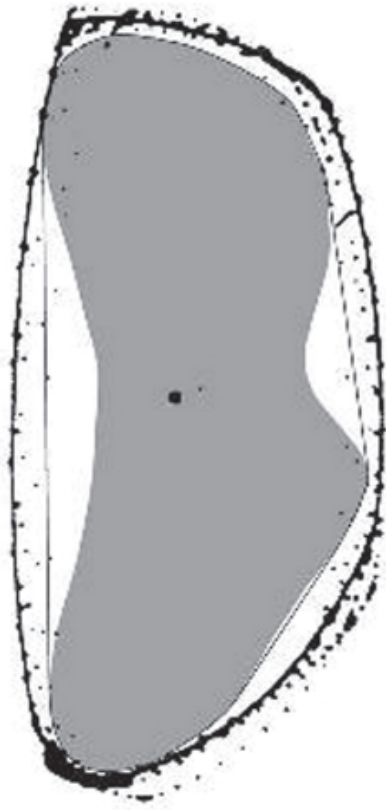


**Fig. 3.** Eros' pole-on silhouette and its convex hull  $H$  compared to the *Ostro et al.* (1990b) estimate of the hull (outermost solid curve) and its associated uncertainty (dots). The radar-derived lower bound on  $H$ 's maximum breadth was 4% larger than the true value and the radar-derived lower bound on  $H$ 's minimum breadth was 0.7% too large.

of the asteroid's surface and interior. A shape model also allows realistic investigation of the effects of collisions in various energy regimes on the object's rotation state, surface topography, regolith, and internal structure (*Asphaug et al.*, 1998). In principle, thorough thermal-infrared observations and modeling of an object for which a radar-derived shape model exists would likely provide fruitful insight into the surface's thermal properties.

### 3. OVERVIEW OF ASTEROID RADAR PROPERTIES

#### 3.1. Polarization Ratio and Radar Albedo

The circular polarization ratio,  $\mu_C = SC/OC$ , can easily be determined upon detection of an asteroid's echoes. Unlike radar cross sections (and hence radar albedos), which are the products of factors that suffer from systematic uncertainties generally on the order of 10%, an estimate of  $SC/OC$  is contaminated almost entirely by statistical error from receiver noise.  $SC/OC$  is a measure of the near-surface structural complexity at scales near the wavelength. An asteroid's  $SC/OC$  can be taken as a crude estimate of its rock

coverage, that is, the fraction of the surface area covered by roughly wavelength-sized rocks.

Constraints on surface properties become increasingly ambiguous and model-dependent as  $SC/OC$  increases from near zero, where single reflections from smooth surface facets dominate the scattering process (e.g., Ceres and Pallas; *Ostro et al.*, 1985), to values of a few tens of percent or larger, indicating increasing contributions from single reflections from rough surfaces and/or multiple scattering. 2101 Adonis, 1992 QN (*Benner et al.*, 1997), 2000 EE104 (*Howell et al.*, 2001), and 33342 (1998 WT24) are the extreme examples, with  $SC/OC$  near unity. The merits of current interpretations of radar properties (albedo, polarization ratio, and scattering law; e.g., *Mitchell et al.*, 1995; *Magri et al.*, 2001) should be clarified upon spacecraft reconnaissance of asteroids for which detailed radar-derived physical models are available.

For  $SC/OC$  near zero, the OC radar albedo ( $\hat{\sigma}_{OC}$ , equal to the OC radar cross section divided by the target's projected area) is a first-order estimate of the Fresnel power reflection coefficient  $R$ , which for most homogeneous materials that are candidates for asteroid surfaces (solid metal is an exception) has been found empirically to depend simply on bulk density  $d_{\text{bulk}}$  (*Magri et al.*, 2001; *Garvin et al.*, 1985; *Olhoeft and Strangway*, 1975)

$$R = \tanh^2(d_{\text{bulk}}/6.4 \text{ g cm}^{-3}) \quad (13)$$

Using the radar properties of Eros and the *NEAR Shoemaker* determination of Eros' L-chondritic composition, *Magri et al.* (2001) have calibrated radar constraints on asteroids' near-surface regolith porosity  $p$ , solid-rock density  $d_{\text{solid}}$ , and bulk density  $d_{\text{bulk}} = (1 - p) d_{\text{solid}}$ .

#### 3.2. Comparison of Main-Belt Asteroids and Near-Earth Asteroids

*Magri et al.* (1999) presented histograms of the distributions of estimates of  $SC/OC$  ratio and OC albedos for 37 MBAs, and *Benner* (2002) lists corresponding data for NEAs. The  $SC/OC$  distribution for NEAs is nonnormal, so nonparametric tests must be used to compare the NEA and MBA distributions. The Mann-Whitney rank-sum test indicates at a high confidence level that these two distributions have different medians; furthermore, the same conclusion holds when C-class objects alone are considered and when S-class objects alone are considered. Levene's test implies that NEAs also exhibit a wider range of polarization ratios than do MBAs, both for the full samples and for S-class targets alone. No such difference in variances can be firmly inferred for C-class objects alone, although we note that only four known C-class NEAs are in the sample. Evidently, most NEA surfaces are moderately or highly complex at decimeter scales, while MBAs are smooth or else moderately rock-covered.

The OC albedo distribution for 19 NEAs with reasonable albedo estimates is statistically similar to that for the 35 MBAs available to *Magri et al.* (1999). The same con-

clusion holds if we compare the distributions for the quantity ( $\hat{\sigma}_{OC} - \hat{\sigma}_{SC}$ ), which represents an attempt to correct for diffuse scattering on the assumption that such scattering produces randomly polarized radiation (Magri et al., 1999; Shepard et al., 2000). If we instead use the quantity ( $\hat{\sigma}_{OC} - 2\hat{\sigma}_{SC}$ ), relevant if diffusely scattered echo power has SC/OC = 1:2 (as is measured for the Moon and inner planets; Harmon and Ostro, 1985), then S-class NEAs and S-class MBAs have different medians, although equal medians still cannot be ruled out when all taxonomic classes are considered.

We conclude that the surfaces of NEAs and MBAs probably differ less strongly in bulk density than in fractional rock coverage. However, we stress the following caveats: First, NEA albedo estimates often are highly uncertain, since very few of the target diameters are well known. Second, in order to obtain Fresnel reflectivity and hence near-surface bulk density, one must correct the OC albedo for the effects of diffuse scattering from wavelength-scale structures, a correction which is large and uncertain for NEAs with high SC/OC.

### 3.3. Comparison of Main-Belt-Asteroid Classes

Statistical analyses of disk-integrated properties of the 37 MBAs observed during 1980–1995 (Magri et al., 1999) indicate that M-class MBAs have higher radar albedos and a wider range of albedos than do MBAs from the other taxonomic classes; there is no evidence that C and S MBAs have different albedo distributions; and there is some suggestion, worthy of future study, that primitive B, F, G, and P MBAs are not as radar-bright as C and S MBAs. There is no statistically significant evidence that different taxonomic classes of MBAs have different polarization ratio distributions, despite suggestions to the contrary based on visual inspection of these distributions. The similarity between the C and S MBA albedo distributions implies similar near-surface regolith bulk densities. The hypothesis of ordinary chondritic composition for the S-class MBAs is reasonably consistent with the radar data, provided that these asteroids have typical lunar porosities. Nevertheless, it is possible that some targets have high-porosity regoliths of stony-iron composition. The M-class MBA sample apparently contains both metallic objects (such as 216 Kleopatra) and stony objects (possibly hydrated, W-class objects; Rivkin et al., 2000).

The high-OC radar albedo ( $0.31 \pm 0.06$ ) of the largest M-class asteroid, 16 Psyche, implies a moderately high near-surface bulk density of  $2.8 (+0.5, -0.6)$  g cm<sup>-3</sup> and hence, if the porosity is about 50%, a grain density within ~20% of  $5.6$  g cm<sup>-3</sup>. The inference of surface bulk density relies on a lab-experimental relationship between microwave reflectivity and bulk density, a relationship which would not apply if Psyche has a solid metal surface; however, it seems hard to believe that such a large object would not retain any fine impact debris on its surface. Magri et al. (1999; see also Ostro et al., 1985) conclude that Psyche is more likely to be a metal-rich object than, say, an enstatite chondrite analog. It is not clear how to reconcile Psyche's

large radar reflectivity with the bulk density,  $1.8 \pm 0.6$  g cm<sup>-3</sup>, implied by the value of Psyche's mass determined astrometrically by Viateau (2000).

## 4. RESULTS FOR SELECTED ASTEROIDS

### 4.1. 4769 Castalia (1989 PB)

A sequence of delay-Doppler images of Castalia (Ostro et al., 1990a) obtained at Arecibo two weeks after its August 1989 discovery reveal it to consist of two kilometer-sized lobes in contact. Least-squares estimation of Castalia's three-dimensional shape from the radar images supports the hypothesis that Castalia is a contact-binary asteroid formed from a gentle collision of the two lobes and also constrains the object's surface morphology and pole direction (Hudson and Ostro, 1994). Analysis of Castalia lightcurves using the radar-derived shape refined the available pole constraints and yielded estimates of average Hapke parameters (Hudson et al., 1997).

### 4.2. 1620 Geographos

Observations of Geographos (Ostro et al., 1995b, 1996) with a nearly equatorial view yielded several hundred images with ~100-m resolution. The pole-on silhouette's extreme dimensions are in a ratio,  $2.76 \pm 0.21$ , that establishes Geographos as the most elongated solar system object imaged so far (Fig. 2). The images show craters as well as indications of other sorts of large-scale topographic relief, including a prominent central indentation. Protuberances at the asteroid's ends may be related to the pattern of ejecta removal and deposition caused by the asteroid's gravity field, or perhaps to tidal effects during a close planetary encounter (Bottke et al., 1999).

### 4.3. 4179 Toutatis

Imaging of Toutatis during its close approaches in 1992 (Ostro et al., 1995a), 1996 (Ostro et al., 1999b), and 2000 achieved resolutions as fine as 125 ns (19 m in range) and 8.3 mHz (0.15 mm/s in radial velocity), placing hundreds to thousands of pixels on the asteroid. Inversion of a low-resolution subset of the 1992 images (Hudson and Ostro, 1995) produced a comprehensive physical model (Fig. 4), including estimates of the asteroid's shape and moment-of-inertia ratios, initial conditions for the asteroid's spin and orientation, the radar-scattering properties of the surface, and the delay-Doppler trajectory of the center of mass. Lightcurves synthesized using that model provide a good fit to optical photometry that spans phase angles from  $0.2^\circ$  to  $121.4^\circ$  (Spencer et al., 1995), and incorporation of the lightcurves in the modeling process slightly refines the spin state (Hudson and Ostro, 1998).

Toutatis is rotating in a long-axis mode characterized by periods of 5.4 d (rotation about the long axis) and 7.4 d (average for long-axis precession about the angular momentum vector); see Scheeres et al. (1998) for a detailed description

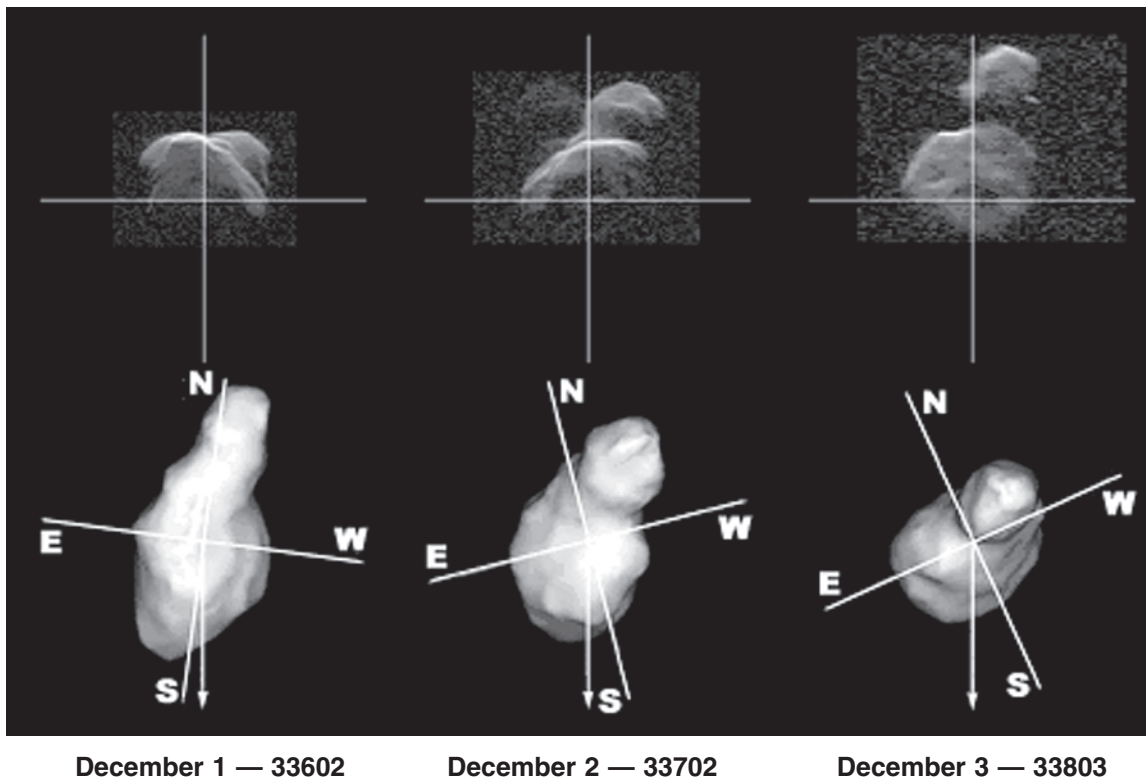


**Fig. 4.** High-resolution delay-Doppler images from each of three observation dates in 1996 and the corresponding plane-of-sky (POS) appearance of *Hudson and Ostro's* (1995) physical model. The cross hairs are 5 km long and centered on Toutatis' center of mass (COM). The radar images are plotted with time delay (range) increasing from top to bottom and Doppler frequency (radial velocity) increasing from left to right. In the POS images, the model is rendered with a Lambertian scattering law, with the viewer and the illumination source colocated. The cross hairs are aligned north-south and east-west on the plane of the sky. In each POS frame, the arrow radiating from the COM shows the POS projection of the instantaneous spin vector.

of the spin state. The asteroid's principal moments of inertia are in ratios within 3% of 3.19 and 3.01, and the inertia tensor is indistinguishable from that of a homogeneous body; such information has yet to be determined for any other asteroid except Eros and probably is impossible to acquire in a fast spacecraft flyby. Dimensions along the principal axes are within 0.10 km of 1.92, 2.40, and 4.60 km. The asteroid's centimeter-to-decameter surface characteristics are strikingly uniform. The disk-integrated, 3.5-cm circular polarization (SC/OC) ratio averages  $0.29 \pm 0.01$  and is independent of orientation at the several percent level.  $SC/OC = 0.25 \pm 0.02$  at 6 cm (*Zaitsev et al.*, 1993). The 3.5-cm OC radar albedo averages  $0.24 \pm 0.03$ ; it depends on orientation, as expected from the asteroid's angular scattering behavior (limb-darkening slightly more than Lambertian). The OC albedo of a sphere with Toutatis' radar properties would be 0.21, or  $3\times$  the lunar value. The radar properties and available nonradar constraints are consistent with Toutatis' surface having a smooth component that is at least one-third covered by rocks at least as large as a decimeter. If this S-class asteroid is mineralogically similar to stony-iron meteorites, then the smooth surface component probably is regolith with porosity resembling that of lunar soil. If the mineralogy is ordinary chondritic, then the smooth

surface component may be nearly solid with not much more than a centimeter of overlying regolith.

The highest-resolution radar images obtained in 1992 and 1996 have been used to construct a Toutatis model consisting of 39,996 triangular facets of roughly equal area, defined by the locations of 20,000 vertices (*R. S. Hudson et al.*, personal communication, 2001). The average spatial resolution of the model is approximately 34 m, significantly finer than the *Hudson and Ostro* (1995) model (1600 vertices, resolution 84 m). The high-resolution model (*Fig. 5*) reveals complex linear features as well as circular crater-like structures down to the resolution limit. The noncrater-like features may be the manifestation of complex interior configurations involving monolithic fragments with various sizes and shapes, presumably due to collisions in various energy regimes.

Given the intensity and outcome of the Toutatis investigations, it may be appropriate to think of that experiment as a flyby of Toutatis by an Earthborne package of radar sensors. A spacecraft flyby would be hundreds of times more expensive than the incremental cost of the radar investigation and would not have been able to determine the asteroid's shape and spin state nearly as well. Obviously, the ratio of cost and risk to science return for a flyby or rendez-



**Fig. 5.** The high-resolution Toutatis model (R. S. Hudson et al., personal communication, 2001) rendered at  $22.5^\circ$  intervals of rotation about the long (x) axis, with illumination coming from within the y-z plane at a  $70^\circ$  angle from the viewer's line of sight.

vous mission (let alone a sample return or a piloted mission) would be dramatically reduced if Toutatis-class radar reconnaissance could be performed on the target in advance.

Toutatis' radar-refined orbit has weighted root-mean-square residuals of 0.98 arcsec,  $1.8 \text{ mm s}^{-1}$  in radial velocity, and 73 m in range. Integration of that orbit into the past and future (Ostro et al., 1999b) shows that Toutatis' pattern of close approaches to Venus, Earth, and Mars is highly asymmetric about the current epoch. The probability of the orbit intersecting the Earth is zero for at least the next six centuries. Toutatis will make its closest planetary approach since at least 1353 and until at least 2562 on September 29, 2004, when the closest COM-to-COM separation of Earth and Toutatis will be  $1,549,834 \pm 10 \text{ km}$  (4.0 lunar distances).

#### 4.4. 6489 Golevka

Goldstone 8510-MHz radar images of Golevka in June 1995 and physical modeling (Hudson et al., 2000a) reveal a half-kilometer object (Plate 2) whose shape is extraordinarily angular, with flat sides, sharp edges and corners, and peculiar concavities. Extremely large gravitational slopes in some areas indicate the presence of exposed, solid, monolithic rock. This asteroid, the first subkilometer object studied in this much detail, is more likely to be a collision fragment than an unconsolidated rubble pile.

The Golevka experiment led to several technical milestones. After three radar-refined generations of orbit solutions during June 3–8, the uncertainty ellipse for the delay-Doppler location of the COM was “inside” the asteroid. The

ephemeris used on June 9, when the asteroid made its closest approach (0.034 AU), was later found to be accurate to 0.01 Hz (a radial velocity of 0.2 mm/s, or about the speed of the tip of a large clock's minute hand). The preliminary model generated on that date was qualitatively almost indistinguishable from the one published by Hudson et al. (2000a). June 13–15 saw the first intercontinental radar astronomy observations, consisting of Goldstone cw transmissions and reception of Golevka's echoes with the Evpatoria (Ukraine) 70-m antenna on each date (Zaitsev et al., 1997) and reception of echoes with the Kashima (Japan) 34-m antenna on June 15 (Koyama et al., 2001). [In 1992, observations with the Evpatoria antenna transmitting and the Effelsberg 100-m antenna receiving had yielded echoes from Toutatis (Zaitsev et al., 1993). In 1999, Golevka echoes from Arecibo transmissions were detected at the Deep Space Network's 70-m DSS-63 antenna near Madrid. In 2001, the Medicina (Italy) 32-m antenna detected echoes from 33342 (1998 WT24) using Goldstone and then Evpatoria transmissions.]

#### 4.5. 4486 Mithra

Images of Mithra reveal a double-lobed object, apparently more severely bifurcated than any other nonbinary NEA imaged to date (Ostro et al., 2000c). The bandwidth of the echoes is consistently very narrow, implying some combination of very slow rotation (evident from the barely noticeable variation in the appearance of images over several hours) and a radar line of sight not far from the apparent spin vector at any time during the experiment; the

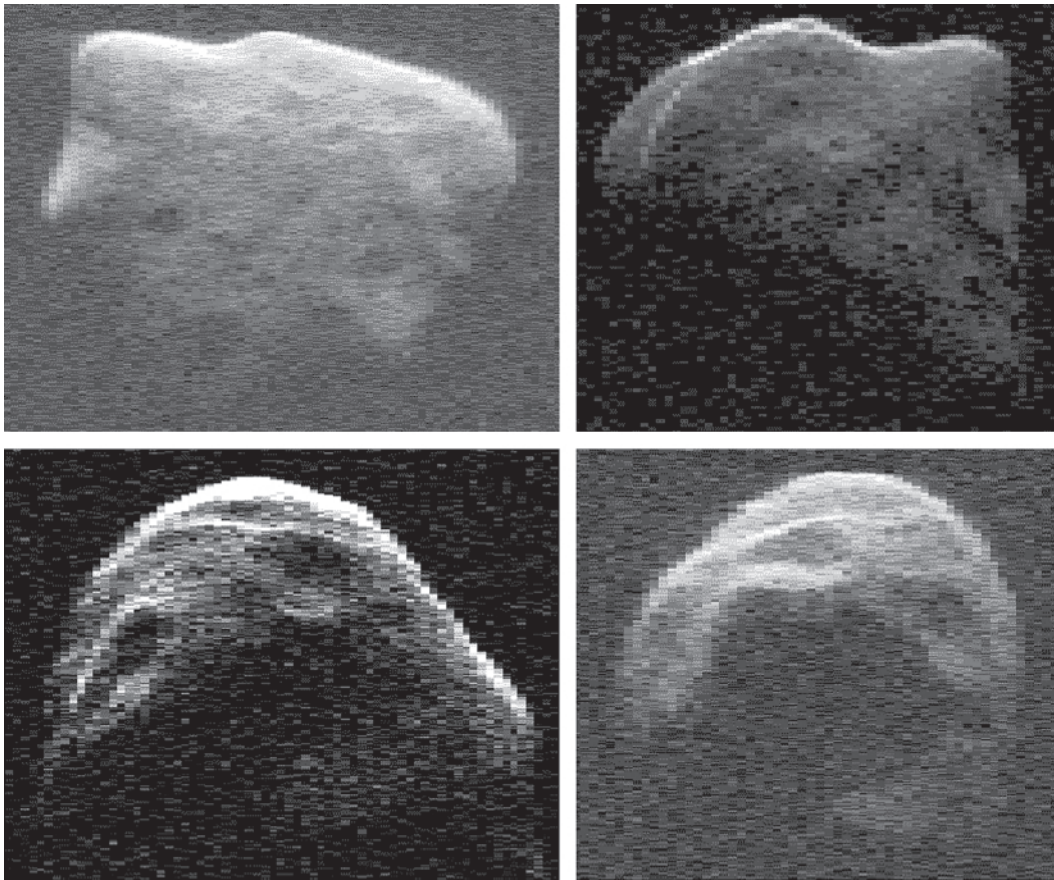


**Fig. 6.** Radar images of 1999 JM8 (*Benner et al.*, 2002a) from Arecibo (top left and bottom right frames) and Goldstone. Radar illumination is from the top. The vertical resolution is 15 m for Arecibo, 38 m in the top Goldstone image, and 19 m in the bottom Goldstone image. The horizontal resolutions depend on the asteroid's spin state, which is not yet known.

radar-observed sky arc was only about  $35^\circ$ . No simple periodicity in the day-to-day image sequence is evident, so nonprincipal-axis rotation is suggested. The alignment of the two lobes is almost parallel to the projected, apparent, instantaneous spin vector in some images but almost perpendicular to it in others, providing additional evidence for a very unusual spin state.

#### 4.6. 1999 JM8

Observations by *Benner et al.* (2002) during this object's discovery apparition (its closest approach until at least 3000) reveal an irregularly shaped object with a maximum dimension that exceeds 5 km and numerous craterlike features with diameters from 100 m to more than 1 km (Fig. 6). 1999 JM8 is in a slow NPA rotation state that may not be very "far" from a PA state. The images provide the strongest evidence to date for a circular polarization ratio feature on an asteroid.

#### 4.7. 1998 KY26

Radar and optical observations (*Ostro et al.*, 1999a) of this NEA shortly after its discovery reveal a slightly elon-

gated, possibly lumpy spheroid with a diameter of about 30 m, a composition analogous to carbonaceous chondritic meteorites, and a rotation period of 10.7 min, which is too rapid for 1998 KY26 to consist of multiple components bound together just by their mutual gravitational attraction. On the other hand, E. Asphaug (personal communication, 1999) has noted that the required tensile strength is very small, comparable to that of snow. 1998 KY26 has the lowest rendezvous  $\Delta V$  (the total change in velocity required to leave low Earth orbit and rendezvous with another body) of any object with a well-known orbit.

#### 4.8. 216 Kleopatra

Radar observations of this M-class asteroid (*Ostro et al.*, 2000a) reveal a dog-bone shape with overall dimensions of  $217 \times 94 \times 81$  km ( $\pm 25\%$ ). The object's high radar albedo, low SC/OC, and gentle gravitational slopes are consistent with a regolith having a metallic composition and a porosity comparable to that of lunar soil. *Ostro et al.* (2000a) argue that Kleopatra's shape is probably the outcome of an exotic sequence of collisional events, and that much of its interior may have an unconsolidated rubble-pile structure.

#### 4.9. 288 Glauke

The combination of Arecibo radar echoes and available visible/infrared data indicates that Glauke is an S-class object slightly smaller and less elongated than 243 Ida, with radar surface properties near the average for S asteroids in the main belt, and in an extraordinarily slow (~50-d) rotation state (Ostro et al., 2001b).

#### 4.10. 1999 GU3

Optical and radar observations (Pravec et al., 2000a) reveal that 1999 GU3 is a subkilometer-sized object with an apparent rotation period of 9 d, low visual and radar albedos, and colors more consistent with the ordinary chondrites than the vast majority of main-belt asteroids.

#### 4.11. 25143 (1998 SF36)

Extensive Arecibo and Goldstone observations of this object were conducted in March–April 2001 in response to its selection as the target of the joint Japanese/NASA MUSES-C sample-return mission. A first look at the images reveals a somewhat ellipsoidal, but asymmetrical, object with overall dimensions of roughly  $0.6 \times 0.3$  km. The surface's small-scale roughness is comparable to Eros', but the surface density appears lower.

#### 4.12. 2063 Bacchus and 3908 Nyx (1980 PA)

Delay-Doppler images of Bacchus (Benner et al., 1999b) reveal an asymmetrical, bifurcated shape with radar-derived dimensions ( $1.1 \times 0.5 \times 0.5$  km) and optical brightness that imply radar and optical albedos among the highest measured for any asteroid, consistent with, for example, a regolith-free basaltic surface. The surface of the basaltic (V-class) object 3908 Nyx is unusually rough at centimeter-to-decimeter scales (Benner et al., 2002b). One or both of these objects may be fragments of Vesta (Binzel and Xu, 1993).

#### 4.13. 7 Iris, 9 Metis, 654 Zelinda, and 12 Victoria

Radar spectra for these large MBAs show evidence for prominent topography: large, flat regions on Iris, Metis, and Zelinda, and a nonconvex, possibly bifurcated shape for Victoria (Mitchell et al., 1995).

#### 4.14. Spheroids

1999 RQ36 (Hudson et al., 2000b), 7822 (1991 CS) (Benner et al., 1999a), 2100 Ra-Shalom (Shepard et al., 2000), 1998 ML14 (Ostro et al., 2001a), 29075 (1950 DA) (Giorgini et al., 2002), and 6037 (1988 EG) have nearly circular pole-on silhouettes. Very strong, well-resolved images of 1999 RQ36 reveal a nearly featureless spheroid. Inversion of images of 1998 ML14 reveals a 1-km spheroid with several-hundred-meter protrusions on one side.

#### 4.15. Very Small Near-Earth Asteroids

As of March 2002, NEAs with  $H > 21$  (corresponding to diameters of ~0.2 km or less) constitute 24/103 or 23% of all radar-detected NEAs (Table 5). Objects in this size range are likely to comprise an increasing percentage of radar-detected NEAs, due to the relatively fast rate at which they are being discovered. Some of these asteroids are comparable in size to boulders seen on the surface of Eros (Veveřka et al., 2001). Most of these objects appear to have rotation periods no longer than an hour, but at least one object, 2001 EC16, is a very slow rotator (J. L. Margot et al., in preparation, 2001). Existing radar systems typically resolve the smallest radar detectable asteroids into only a few range pixels or less, so much of the leverage for shape modeling will have to come from Doppler resolution.

#### 4.16. Binary Near-Earth Asteroids

Goldstone and Arecibo delay-Doppler observations during September 2000 to October 2001 revealed that 2000 DP107, 2000 UG11, 1999 KW4, 1998 ST27, and 2002 BM26 are binary systems. For 2000 DP107 (Margot et al., 2002), images show separations up to at least 1 km between the components, which have different sizes and rotation states. Estimates of the diameters based on range extents are 800 m and 300 m for the primary and secondary respectively. Preliminary fits to delay-Doppler data indicate an orbital period of 1.7 d and a semimajor axis of 2.6 km (uncertainties ~10%). These parameters imply that the density of the primary is about  $1.7 \text{ g cm}^{-3}$ . For 2000 UG11 (Nolan et al., 2001), preliminary estimates of average diameters, based on range extents at 15-m resolution, are 230 and 100 m. The components' maximum separation is more than 300 m and its orbital period is  $19 \pm 1.5$  h. For 1999 KW4, very thorough, high-SNR, decimeter-resolution delay-Doppler images should characterize the components and their dynamics in detail. The images (e.g., Fig. 7) show separations up to at least 2 km between the components, whose sizes differ by a factor of about 3 (Benner et al., 2001a; S. Ostro et al., in preparation, 2002). Initial analysis suggests that the density of the primary is between  $1.8$  and  $3.0 \text{ g cm}^{-3}$ . For 1998 ST27, the images show separations up to at least 4 km between the components, whose sizes differ by a factor of at least 3 (Benner et al., 2001b).

### 5. CHALLENGES FOR THE COMING DECADE

#### 5.1 Telescope Time

Both Arecibo and Goldstone are heavily oversubscribed (as foreseen; Ostro, 1994). Additionally, numerous NEA opportunities at Goldstone are lost due to airspace clearance protocols that require all transmissions to be approved by military and civilian authorities. During the past few years, Arecibo was used for radar astronomy 8% of the time, of which more than half was for asteroids. DSS-14

TABLE 5. Very small radar-detected near-Earth asteroids.

Asteroid	H (mag)	$D_{\text{radar}}$ (m)	$D_C$ (m)	$D_S$ (m)	Period (h)	SC/OC	Reference*
1998 BY7	21.5	NA	300	150	<1.3	$0.4 \pm 0.04$	Ostro et al.
1998 KY26	25.5	30	48	24	0.18	$0.5 \pm 0.1$	Ostro et al. (1999a)
1999 FN19	22.4	110	190	95	<11	$0.22 \pm 0.01$	Benner et al.
1999 NW2	23.1	NA	150	72	<4.2	$0.35 \pm 0.02$	Benner et al.
1999 TN13	23.6	NA	120	57	<1.3		Benner et al.
1999 TY2	23.3	NA	130	66	0.12		Pravec et al. (2000b)
2000 EH26	21.2	120	260	130	<33		Benner et al. (2001a)
2000 EW70	21.1	360	360	180	<33		Margot et al.
2000 LF3	21.6	NA	300	150	<1.0	<0.2	Nolan et al.
2000 PH5	22.3	120	170	90	0.29	$0.29 \pm 0.02$	Margot et al.
2000 UK11	25.0	<60	52	26	~0.05		Nolan et al. (2001)
2000 YA	23.7	120	110	52	<1.3		Benner et al. (2001a)
2001 AV43	24.3	NA	72	36	?		Nolan et al.
2001 BF10	22.3	NA	170	83	<0.4		Howell et al.
2001 CP36	23.7	90	110	55	slow?	~1.0	Nolan et al.
2001 EC16	22.2	150	200	100	slow	~0.2	Margot et al. (2001)
2001 FR85	24.5	?	79	40	?		Nolan et al.
2001 JV1	21.3	?	320	160	<29		Ostro et al.
2001 SP263	25.8	?	42	21	?		Nolan et al.
2001 UP	25.7	?	44	22	?		Nolan et al.
2001 WM15	25.0	?	60	30	?		Nolan et al.
2001 XX4	21.9	?	250	130	?		Nolan et al.
2001 YP3	21.9	?	250	130	?		Nolan et al.
2002 AV	20.7	?	380	190	?		Ostro et al.
2002 FD6	22.3	110	210	110	?		Benner et al.

\*References without dates are in preparation.

Objects with  $H > 21$  (suggesting diameters less than about 200 m) are listed along with constraints on diameter, rotation period, and circular polarization ratio.  $D_{\text{radar}}$  is twice the echoes' range extent except for 1998 KY26, for which a shape model is available. For some objects, range-resolved data are not available (NA).  $D_C$  and  $D_S$  are diameters corresponding to typical optical geometric albedos  $p_v$  for the C ( $p_v = 0.05$ ) and S ( $p_v = 0.20$ ) classes, calculated using the equation  $\log p_v = 6.259 - \log D - 0.4 H$ , from *Bowell et al.* (1989). For objects other than 1998 KY26 and 1999 TY2, we combined  $D_C$  with the echo bandwidth to set an upper bound on the period. For 1999 NW2, photometric colors (M. Hicks, personal communication, 1999) suggest an SQ classification, so we combined  $D_S$  with the echo bandwidth to set an upper bound on the period.

was used for radar astronomy 6% of the time, of which less than half was for asteroids. These percentages are unlikely to increase much, and they certainly cannot keep up with the NEA discovery rate. Even now, only about half of asteroid radar time requests are allocated. NPA rotators are generally very slow, so many days of observations are required for a unique spin-state solution to be tractable. Thus, limitations on telescope time allocation undermine characterization of objects in the most interesting spin states. Perhaps it is time to propose a dedicated asteroid radar with 10 $\times$  the sensitivity of Arecibo, whose ~\$200 million cost would be comparable to that of a Discovery mission (*Ostro*, 1997).

## 5.2. Multiantenna Observations and Interferometry

The potential of the recently completed 100-m Greenbank Telescope (GBT, part of the National Radio Astronomy Observatory, NRAO) as the receiving antenna in "bi-

static" radar experiments is both promising and challenging.

The Arecibo-GBT configuration, which already has yielded a detection of 2000 EC16 (J. L. Margot et al., in preparation, 2001), will permit more lucrative observations of very close and/or narrowband (very small or slowly rotating) NEAs than would be possible with Arecibo monostatically. Goldstone-GBT observations will enjoy a tenfold increase in sensitivity over the DSS-14-to-DSS-13 configuration. However, apart from the logistics of securing antenna time on two institution's instruments, establishment of an unbiased system for accurate delay astrometry will be more difficult than it was for the DSS-14-to-DSS-13 system, which has a fiber-optics linkage. Similar comments apply to 2380-MHz Arecibo-Goldstone observations, which have been conducted several times; observations involving Arecibo and the 25-m VLBA antenna on St. Croix, which have been used for bistatic imaging of the Moon; and 8560-MHz Goldstone-Arecibo observations, which are planned. This chapter was finalized right after completion of a three-week

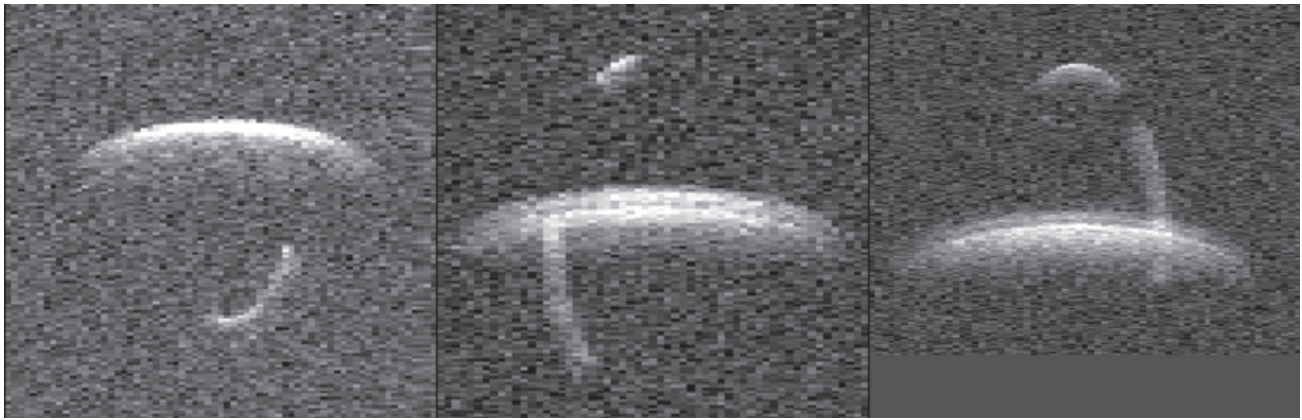


**Fig. 7.** Several-hour delay-Doppler time exposures of radar echoes from binary asteroid 1999 KW4 (S. Ostro et al., in preparation, 2002). Distance from Earth increases toward the bottom, and speed from Earth increases toward the left. The motion of the secondary (smaller) component about the primary (larger) component is clockwise. Gaps in the trail are due to breaks in the data-taking. The primary appears much wider than the secondary because it is a few times bigger and is rotating much faster. Although the components have the same speeds along the radar line of sight and the same distances from the radar where their echoes overlap, their positions in space are never the same. The components orbit a common center of mass, and each component's average distance from that point is inversely proportional to its mass. The motion of the relatively massive primary is much less obvious than the motion of the secondary, but can be seen in the double appearance of the primary's top edge in the two time exposures that follow the secondary from in front of the primary to behind it. These Goldstone (8560-MHz, 3.5-cm) images have overall extents of  $37.5 \mu\text{s} \times 67 \text{ Hz}$  ( $5.6 \text{ km} \times 1.2 \text{ m s}^{-1}$ ).

experiment on 38071 (1999 GU3) incorporating Arecibo-GBT and Goldstone-GBT delay-Doppler imaging (L. A. M. Benner et al., in preparation, 2002).

Aperture-synthesis observations using transmission from Goldstone and reception at the 27-antenna Very Large Array (VLA) achieved marginal resolution of 324 Bamberga and 7 Iris (*de Pater et al.*, 1994) and helped to constrain their pole directions. Goldstone-VLA detections of Toutatis by the same authors and of Golevka by *Hudson et al.* (2000) provided POS astrometry that is roughly comparable in accuracy with the best traditional optical astrometry, that is, when Hipparcos-based reference catalogs are used in the reductions.

Apart from the Goldstone-VLA work, all useful asteroid radar imaging has relied on delay/Doppler resolution. In principle, interferometric methods can make radar images with very fine angular resolution, similar to optical pictures and free from the ambiguities that afflict delay-Doppler images. The VLA's longest baseline is 36.4 km and its finest achievable angular resolution at 8560 MHz is 0.24 arcsec. Enlargement of the array could shrink the resolution by nearly an order of magnitude. The Very Long Baseline Array (VLBA) has a maximum baseline of 8611 km and in principle can achieve a resolution at 8560 MHz of 0.85 milli-arcsec. Arecibo-VLBA echoes from 2000 EW70 (G. J. Black et al., in preparation, 2001) have been detected, but actual VLBA radar images of asteroids have yet to be constructed for any object. *Koyama et al.* (2001) attempted interferometric observations of 4197 1982 TA using Goldstone transmissions and reception at the Kashima and Usuda antennas in Japan, but analysis of the echoes was inconclusive. Single baseline interferometry has been at-

tempted with Golevka (Arecibo-Madrid), 1999 RQ36 (Arecibo-Goldstone), and 1999 KW4 (Arecibo-Goldstone); see *Margot and Nolan* (1999). Although interferometric techniques are logistically daunting, their promise is considerable. Perhaps the most tantalizing experiment would be a multiday sequence of simultaneous delay-Doppler images and radar interferometric images of a comet nucleus and coma at very high echo strength.

### 5.3. Data Interpretation

Reconstruction of physical models from delay-Doppler images has proved to be relatively straightforward for uniform rotators but horribly difficult for NPA rotators because of the size of the parameter space. This estimation problem demands serious attention.

*Vokrouhlický et al.* (2000) have suggested that the existence of precise radar astrometry of certain asteroids at multiple apparitions might reveal orbit perturbations resulting from the Yarkovsky effect, a subtle nongravitational phenomenon related to anisotropic thermal emission from the asteroid's surface. They list several opportunities for acquiring such data during the next few decades. The associated covariance space, especially the coupling between constraints on the Yarkovsky effect and constraints on asteroid thermal behavior, indicates that definitive conclusions will require modeling of the effect using the actual shape and spin state of any candidate target, with a suitably parameterized thermal model.

Integration of the radar + optical orbit of 29075 (1950 DA) (*Giorgini et al.*, 2001) has indicated a very close approach to Earth (with a small possibility of impact) in March 2880

that was not evident in solutions based solely on initial optical data. The associated uncertainties depend primarily on the Yarkovsky acceleration, which depends on the object's shape, spin state, and thermal properties. This situation dramatizes the fundamental coupling between the physical properties of NEAs and long-term prediction of their trajectories, as well as the value of radar astrometry for orbit determination.

The radar discovery of NEA binary systems presents the challenge of extracting physical and dynamical properties from the echoes. Delay-Doppler images are taken in a coordinate system tied to the planetary ephemerides, so one can determine the orbits of the components relative to the system's center of mass as well as relative to each other. Thus the components' mass and density ratios as well as their total mass can be derived. Optimum estimation procedures need to be developed and supported by appropriate covariance studies. Ideally, one would merge the results with both shape estimation and heliocentric orbit refinement procedures to construct a single, comprehensive estimator for all the relevant physical and dynamical parameters for single and multiple bodies.

## REFERENCES

- Andrews A. K., Hudson R. S., and Psaltis D. (1995) Optical-radar imaging of scale models for studies in asteroid astronomy. *Optics Lett.*, 20, 2327–2329.
- Asphaug E., Ostro S. J., Hudson R. S., Scheeres D. J., and Benz W. (1998) Disruption of kilometre-sized asteroids by energetic collisions. *Nature*, 393, 437–440.
- Benner L. A. M. (2002) Summaries of asteroid radar properties [on line]. California Institute of Technology, Pasadena [cited June 1, 2002]. Available on line at [http://echo.jpl.nasa.gov/~lance/asteroid\\_radar\\_properties.html](http://echo.jpl.nasa.gov/~lance/asteroid_radar_properties.html).
- Benner L. A. M., Ostro S. J., Giorgini J. D., Jurgens R. F., Mitchell D. L., Rose R., Rosema K. D., Slade M. A., Winkler R., Yeomans D. K., Campbell D. B., Chandler J. F., and Shapiro I. I. (1997) Radar detection of near-Earth asteroids 2062 Aten, 2101 Adonis, 3103 Eger, 4544 Xanthus, and 1992 QN. *Icarus*, 130, 296–312.
- Benner L. A. M., Ostro S. J., Rosema K. D., Giorgini J. D., Choate D., Jurgens R. F., Rose R., Slade M. A., Thomas M. L., Winkler R., and Yeomans D. K. (1999a) Radar observations of asteroid 7822 (1991 CS). *Icarus*, 137, 247–259.
- Benner L. A. M., Hudson R. S., Ostro S. J., Rosema K. D., Giorgini J. D., Yeomans D. K., Jurgens R. F., Mitchell D. L., Winkler R., Rose R., Slade M. A., Thomas M. L., and Pravec P. (1999b) Radar observations of asteroid 2063 Bacchus. *Icarus*, 139, 309–327.
- Benner L. A. M., Ostro S. J., Giorgini J. D., Jurgens R. F., Margot J. L., and Nolan M. C. (2001a) 1999 KW4. IAU Circular 7632.
- Benner L. A. M., Ostro S. J., Giorgini J. D., Jurgens R. F., Margot J. L., and Nolan M. C. (2001b) 1998 ST27. IAU Circular 7730.
- Benner L. A. M., Ostro S. J., Nolan M. C., Margot J.-L., Giorgini J. D., Hudson R. S., Jurgens R. F., Slade M. A., Howell E. S., Campbell D. B., and Yeomans D. K. (2002a) Radar observations of asteroid 1999 JM8. *Meteoritics & Planet. Sci.*, 37, 779–792.
- Benner L. A. M., Ostro S. J., Hudson R. S., Rosema K. D., Jurgens R. F., Yeomans D. K., Campbell D. B., Chandler J. F., and Shapiro I. I. (2002b) Radar observations of asteroid 3908 Nyx. *Icarus*, 158, in press.
- Binzel R. P. and Xu S. (1993) Chips off of asteroid 4 Vesta — Evidence for the parent body of basaltic achondrite. *Science*, 260, 186–191.
- Binzel R. P., Gehrels T., and Matthews M. S., eds. (1989) *Asteroids II*. Univ. of Arizona, Tucson. 1258 pp.
- Botke W. F. Jr., Richardson D. C., and Love S. G. (1999) 1620 Geographos and 433 Eros: Shaped by planetary tides? *Astron. J.*, 117, 1921–1928.
- Bowell E., Hapke B., Domingue D., Lumme K., Peltoniemi J., and Harris A. W. (1989) Application of photometric models to asteroids. In *Asteroids II* (R. P. Binzel et al., eds.), pp. 524–556. Univ. of Arizona, Tucson.
- de Pater I., Palmer P., Mitchell D. L., Ostro S. J., Yeomans D. K., and Snyder L. E. (1994) Radar aperture synthesis observations of asteroids. *Icarus*, 111, 489–502.
- Garvin J. B., Head J. W., Pettengill G. H. and Zisk S. H. (1985) Venus global radar reflectivity and correlations with elevation. *J. Geophys. Res.*, 90, 6859–6871.
- Giorgini J. D. (2002) Small-Body Astrometric Radar Observations [on line]. California Institute of Technology, Pasadena [cited June 1, 2002]. Available on line at [http://ssd.jpl.nasa.gov/radar\\_data.html](http://ssd.jpl.nasa.gov/radar_data.html).
- Giorgini J. D., Ostro S. J., Benner L. A. M., Chodas P. W., Chesley S. R., Hudson R. S., Nolan M. C., Klemola A. R., Standish E. M., Jurgens R. F., Rose R., Chamberlin A. B., Yeomans D. K., and Margot J.-L. (2002) Asteroid 1950 DA's encounter with Earth in 2880: Physical limits of collision probability prediction. *Science*, 296, 132–136.
- Harmon J. K. and Ostro S. J. (1985) Mars: Dual-polarization radar observations with extended coverage. *Icarus*, 62, 110–128.
- Harmon J. K., Campbell D. B., Ostro S. J., and Nolan M. C. (1999) Radar observations of comets. *Planet. Space Sci.*, 47, 1409–1422.
- Harris A. W. (1994) Tumbling asteroids. *Icarus*, 107, 209–211.
- Howell E. S., Nolan M. C., DeRemer L., and Margot J.-L. (2001) Arecibo radar observations of near-Earth asteroid 2000 EE104 (abstract). *Bull. Am. Astron. Soc.*, 33, 1153.
- Hudson S. (1993) Three-dimensional reconstruction of asteroids from radar observations. *Remote Sens. Rev.*, 8, 195–203.
- Hudson R. S. and Ostro S. J. (1994) Shape of asteroid 4769 Castalia (1989 PB) from inversion of radar images. *Science*, 263, 940–943.
- Hudson R. S. and Ostro S. J. (1995) Shape and non-principal-axis spin state of asteroid 4179 Toutatis from radar images. *Science*, 270, 84–86.
- Hudson R. S. and Ostro S. J. (1998) Photometric properties of asteroid 4179 Toutatis from lightcurves and a radar-derived physical model. *Icarus*, 135, 451–457.
- Hudson R. S. and Ostro S. J. (1999) Physical model of asteroid 1620 Geographos from radar and optical data. *Icarus*, 140, 369–378.
- Hudson R. S., Ostro S. J., and Harris A. W. (1997) Constraints on spin state and Hapke parameters of asteroid 4769 Castalia using lightcurves and a radar-derived shape model. *Icarus*, 130, 165–176.
- Hudson R. S., Ostro S. J., Jurgens R. F., Rosema K. D., Giorgini J. D., Winkler R., Rose R., Choate D., Cormier R. A., Franck C. R., Frye R., Howard D., Kelley D., Littlefair R., Slade

- M. A., Benner L. A. M., Thomas M. L., Mitchell D. L., Chodas P. W., Yeomans D. K., Scheeres D. J., Palmer P., Zaitsev A., Koyama Y., Nakamura A., Harris A. W., and Meshkov M. N. (2000a) Radar observations and physical modeling of asteroid 6489 Golevka. *Icarus*, 148, 37–51.
- Hudson R. S., Ostro S. J., and Benner L. A. M. (2000b) Recent delay-Doppler radar asteroid modeling results: 1999 RQ36 and craters on Toutatis (abstract). *Bull. Am. Astron. Soc.*, 32, 1001.
- Jenkins G. M. and Watts D. G. (1968) *Spectral Analysis and Its Applications*. Holden-Day, San Francisco. 525 pp.
- Jurgens R. F. and Goldstein R. M. (1976) Radar observations at 3.5 and 12.6 cm wavelength of asteroid 433 Eros. *Icarus*, 28, 1–15.
- Koyama Y., Nakajima J., Sekido M., Yoshikawa M., Nakamura A. M., Hirabayashi H., Okada T., Abe M., Nishibori T., Fuse T., Ostro S. J., Choate D., Cormier R. A., Winkler R., Jurgens R. F., Giorgini J. D., Yeomans D. K., Slade M. A., and Zaitsev A. L. (2001) Radar observations of near Earth asteroids 6489 Golevka and 4197 (1982 TA). *J. Comm. Res. Lab.*, 48, 143–150.
- Magri C., Ostro S. J., Rosema K. D., Mitchell D. L., Campbell D. B., Chandler J. F., Shapiro I. I., Giorgini J. D., and Yeomans D. K. (1999) Mainbelt asteroids: Results of Arecibo and Goldstone radar observations of 37 objects during 1980–1995. *Icarus*, 140, 379–407.
- Magri C., Consolmagno G. J., Ostro S. J., Benner L. A. M., and Beeny B. R. (2001) Radar constraints on asteroid regolith compositions using 433 Eros as ground truth. *Meteoritics & Planet. Sci.*, 36, 1697–1709.
- Margot J.-L. and Nolan M. C. (1999) Radar interferometric imaging of near-Earth asteroids (abstract). *Bull. Am. Astron. Soc.*, 31, 2002.
- Margot J. L., Nolan M. C., Benner L. A. M., Ostro S. J., Jurgens R. F., Slade M. A., Giorgini J. D., and Campbell D. B. (2000) *Satellites of Minor Planets*. IAU Circular 7503.
- Margot J. L., Nolan M. C., Benner L. A. M., Ostro S. J., Jurgens R. F., Giorgini J. D., Slade M. A., and Campbell D. B. (2002) Binary asteroids in the near-Earth object population. *Science*, 296, 1445–1448.
- Mitchell D. L., Ostro S. J., Rosema K. D., Hudson R. S., Campbell D. B., Chandler J. F., and Shapiro I. I. (1995) Radar observations of asteroids 7 Iris, 9 Metis, 12 Victoria, 216 Kleopatra, and 654 Zelinda. *Icarus*, 118, 105–131.
- Mitchell D. L., Ostro S. J., Hudson R. S., Rosema K. D., Campbell D. B., Velez R., Chandler J. F., Shapiro I. I., Giorgini J. D., and Yeomans D. K. (1996) Radar observations of asteroids 1 Ceres, 2 Pallas, and 4 Vesta. *Icarus*, 124, 113–133.
- Mitchell D. L., Hudson R. S., Ostro S. J., and Rosema K. D. (1998) Shape of asteroid 433 Eros from inversion of Goldstone radar Doppler spectra. *Icarus*, 131, 4–14.
- Nolan M. C., Margot J.-L., Howell E. S., Benner L. A. M., Ostro S. J., Jurgens R. F., Giorgini J. D., and Campbell D. B. (2001) Radar observations of near-Earth asteroids 2000 UG11 and 2000 UK11 (abstract). In *Lunar and Planetary Science XXXII*, Abstract #2055. Lunar and Planetary Institute, Houston (CD-ROM).
- Olhoef G. R. and Strangway D. W. (1975) Electrical properties of the first 100 meters of the moon. *Earth Planet. Sci. Lett.*, 24, 394–404.
- Ostro S. J. (1989) Radar observations of asteroids. In *Asteroids II* (R. P. Binzel et al., eds.), pp. 192–212. Univ. of Arizona, Tucson.
- Ostro S. J. (1993) Planetary radar astronomy. *Rev. Mod. Phys.*, 65, 1235–1279.
- Ostro S. J. (1994) The role of groundbased radar in near-Earth object hazard identification and mitigation. In *Hazards Due to Comets and Asteroids* (T. Gehrels, ed.), pp. 259–282. Univ. of Arizona, Tucson.
- Ostro S. J. (1997) Radar reconnaissance of near-Earth objects at the dawn of the next millennium. In *Near-Earth Objects: The United Nations International Conference* (J. Remo, ed.), pp. 118–139. Annals of the New York Academy of Sciences, Vol. 822.
- Ostro S. J. (2002a) Radar-Detected Asteroids [on line]. California Institute of Technology, Pasadena [cited June 1, 2002]. Available on line at <http://echo.jpl.nasa.gov/asteroids/index.html>.
- Ostro S. J. (2002b) Planetary radar astronomy. In *The Encyclopedia of Physical Science and Technology, 3rd Edition, Vol. 12* (R. A. Meyers, ed.), pp. 295–328. Academic, New York.
- Ostro S. J. and Connelly R. (1984) Convex profiles from asteroid lightcurves. *Icarus*, 57, 443–463.
- Ostro S. J., Campbell D. B., and Shapiro I. I. (1983) Radar observations of asteroid 1685 Toro. *Astron. J.*, 88, 565–576.
- Ostro S. J., Campbell D. B., and Shapiro I. I. (1985) Mainbelt asteroids: Dual-polarization radar observations. *Science*, 229, 442–446.
- Ostro S. J., Connelly R., and Belkora L. (1988) Asteroid shapes from radar echo spectra: A new theoretical approach. *Icarus*, 73, 15–24.
- Ostro S. J., Chandler J. F., Hine A. A., Shapiro I. I., Rosema K. D., and Yeomans D. K. (1990a) Radar images of asteroid 1989 PB. *Science*, 248, 1523–1528.
- Ostro S. J., Rosema K. D., and Jurgens R. F. (1990b) The shape of Eros. *Icarus*, 84, 334–351.
- Ostro S. J., Campbell D. B., Hine A. A., Shapiro I. I., Chandler J. F., Werner C. L., and Rosema K. D. (1990c) Radar images of asteroid 1627 Ivar. *Astron. J.*, 99, 2012–2018.
- Ostro S. J., Campbell D. B., Chandler J. F., Shapiro I. I., Hine A. A., Velez R., Jurgens R. F., Rosema K. D., Winkler R., and Yeomans D. K. (1991a) Asteroid radar astrometry. *Astron. J.*, 102, 1490–1502.
- Ostro S. J., Campbell D. B., Chandler J. F., Hine A. A., Hudson R. S., Rosema K. D., and Shapiro I. I. (1991b) Asteroid 1986 DA: Radar evidence for a metallic composition. *Science*, 252, 1399–1404.
- Ostro S. J., Hudson R. S., Jurgens R. F., Rosema K. D., Winkler R., Howard D., Rose R., Slade M. A., Yeomans D. K., Giorgini J. D., Campbell D. B., Perillat P., Chandler J. F., and Shapiro I. I. (1995a) Radar images of asteroid 4179 Toutatis. *Science*, 270, 80–83.
- Ostro S. J., Rosema K. D., Hudson R. S., Jurgens R. F., Giorgini J. D., Winkler R., Yeomans D. K., Choate D., Rose R., Slade M. A., Howard S. D., and Mitchell D. L. (1995b) Extreme elongation of asteroid 1620 Geographos from radar images. *Nature*, 375, 474–477.
- Ostro S. J., Jurgens R. F., Rosema K. D., Hudson R. S., Giorgini J. D., Winkler R., Yeomans D. K., Choate D., Rose R., Slade M. A., Howard S. D., Scheeres D. J., and Mitchell D. L. (1996) Radar observations of asteroid 1620 Geographos. *Icarus*, 121, 44–66.
- Ostro S. J., Pravec P., Benner L. A. M., Hudson R. S., Šarounová L., Hicks M. D., Rabinowitz D. L., Scotti J. V., Tholen D. J., Wolf M., Jurgens R. F., Thomas M. L., Giorgini J. D., Chodas P. W., Yeomans D. K., Rose R., Frye R., Rosema K. D., Winkler R., and Slade M. A. (1999a) Radar and optical observations of asteroid 1998 KY26. *Science*, 285, 557–559.

- Ostro S. J., Hudson R. S., Rosema K. D., Giorgini J. D., Jurgens R. F., Yeomans D. K., Chodas P. W., Winkler R., Rose R., Choate D., Cormier R. A., Kelley D., Littlefair R., Benner L. A. M., Thomas M. L., and Slade M. A. (1999b) Asteroid 4179 Toutatis: 1996 radar observations. *Icarus*, *137*, 122–139.
- Ostro S. J., Hudson R. S., Nolan M. C., Margot J.-L., Scheeres D. J., Campbell D. B., Magri C., Giorgini J. D., and Yeomans D. K. (2000a) Radar observations of asteroid 216 Kleopatra. *Science*, *288*, 836–839.
- Ostro S. J., Hudson R. S., and Thomas P. C. (2000b) Evaluation of radar constraints on the shape of Eros (abstract). *Eos Trans. AGU*, *81*, F771.
- Ostro S. J., Hudson R. S., Benner L. A. M., Nolan M. C., Margot J.-L., Giorgini J. D., Jurgens R. F., Rose R., Yeomans D. K. (2000c) Radar observations of asteroid 4486 Mithra (abstract). *Bull. Am. Astron. Soc.*, *32*, 1003.
- Ostro S. J., Hudson R. S., Benner L. A. M., Nolan M. C., Giorgini J. D., Scheeres D. J., Jurgens R. F., and Rose R. (2001a) Radar observations of asteroid 1998 ML14. *Meteoritics & Planet. Sci.*, *36*, 1225–1236.
- Ostro S. J., Nolan M. C., Margot J.-L., Magri C., Harris A. W., and Giorgini J. D. (2001b) Radar observations of asteroid 288 Glauke. *Icarus*, *152*, 201–204.
- Ostro S. J., Rosema K. D., Campbell D. B., and Shapiro I. I. (2002) Radar observations of asteroid 1862 Apollo. *Icarus*, *156*, 580–583.
- Pravec P., Šarounová L., Benner L. A. M., Ostro S. J., Hicks M. D., Jurgens R. F., Giorgini J. D., Slade M. A., Yeomans D. K., Rabinowitz D. L., Krugly Y. N., and Wolf M. (2000a) Slowly rotating asteroid 1999 GU3. *Icarus*, *148*, 589–593.
- Pravec P., Hergenrother C., Whiteley R., Šarounová L., Kušnirák P., and Wolf M. (2000b) Fast rotating asteroids 1999 TY2, 1999 SF10, and 1998 WB2. *Icarus*, *147*, 477–486.
- Rivkin A. S., Howell E. S., Lebofsky L. A., Clark B. E., and Britt D. T. (2000) The nature of M-class asteroids from 3-mm observations. *Icarus*, *145*, 351–368.
- Scheeres D. J., Ostro S. J., Hudson R. S., and Werner R. A. (1996) Orbits close to asteroid 4769 Castalia. *Icarus*, *121*, 67–87.
- Scheeres D. J., Ostro S. J., Hudson R. S., Suzuki S., and de Jong E. (1998) Dynamics of orbits close to asteroid 4179 Toutatis. *Icarus*, *132*, 53–79.
- Scheeres D. J., Ostro S. J., Werner R. A., Asphaug E., and Hudson R. S. (2000) Effects of gravitational interactions on asteroid spin states. *Icarus*, *147*, 106–118.
- Shepard M. K., Benner L. A. M., Ostro S. J., Harris A. W., Rosema K. D., Shapiro I. I., Chandler J. F., and Campbell D. B. (2000) Radar observations of 2100 Ra-Shalom. *Icarus*, *147*, 520–529.
- Spencer J. R., Akimov L. A., Angeli C., Angelini P., Barucci M. A., Birch P., Blanco C., Buie M. W., Caruso A., Chiornij V. G., Colas F., Dentshev P., Dorokhov N. I., de Sanctis M. C., Dotto E., Ezhkova O. B., Fulchignoni M., Green S., Harris A. W., Howell E. S., Hudecek T., Kalashnikov A. V., Kobelev V. V., Korobova Z. B., Koshkin N. I., Kozhevnikov V. P., Krugly Y. N., Lazzaro D., Lecacheux J., MacConnell J., Mel'nikov S. Y., Michałowski T., Mueller B. E. A., Nakamura T., Neese C., Nolan M. C., Osborn W., Pravec P., Riccioli D., Shevchenko V. S., Shevchenko V. G., Tholen D. J., Velichko F. P., Venditti C., Venditti R., Wisniewski W., Young J., and Zellner B. (1995) The lightcurve of 4179 Toutatis: Evidence for complex rotation. *Icarus*, *117*, 71–89.
- Veverka J., Robinson M., Thomas P., Murchie S., Bell J. F., Izenberg N., Chapman C., Harch A., Bell M., Carcich B., Cheng A., Clark B., Domingue D., Dunham D., Farquhar R., Gaffey M. J., Hawkins E., Joseph J., Kirk R., Li H., Lucey P., Malin M., Martin P., McFadden L., Merline W. J., Miller J. K., Owen W. M., Peterson C., Prockter L., Warren J., Wellnitz D., Williams B. G., Yeomans D. K. (2000) NEAR at Eros: Imaging and spectral results. *Science*, *289*, 2088–2097.
- Veverka J., Thomas P. C., Robinson M., Murchie S., Chapman C., Bell M., Harch A., Merline W. J., Bell J. F., Bussey B., Carcich B., Cheng A., Clark B., Domingue D., Dunham D., Farquhar R., Gaffey M. J., Hawkins E., Izenberg N., Joseph J., Kirk R., Li H., Lucey P., Malin M., McFadden L., Miller J. K., Owen W. M., Peterson C., Prockter L., Warren J., Wellnitz D., Williams B. G., and Yeomans D. K. (2001) Imaging of small-scale features of 433 Eros from NEAR: Evidence for a complex regolith. *Science*, *292*, 484–488.
- Viateau B. (2000) Mass and density of asteroids (16) Psyche and (121) Hermione. *Astron. Astrophys.*, *354*, 725–731.
- Vokrouhlický D., Milani A., and Chesley S. R. (2000) Yarkovsky effect on small near-Earth asteroids: Mathematical formulation and examples. *Icarus*, *148*, 118–138.
- Yeomans D. K., Ostro S. J., and Chodas P. W. (1987) Radar astrometry of near-Earth asteroids. *Astron. J.*, *94*, 189–200.
- Yeomans D. K., Chodas P. W., Keesey M. S., Ostro S. J., Chandler J. F., and Shapiro I. I. (1992) Asteroid and comet orbits using radar data. *Astron. J.*, *103*, 303–317.
- Zaitsev A. L., Sokolsky A. G., Rzhiga O. R., Vyshlov A. S., Krivtsov A. P., and Shubin V. A. (1993) Radar investigation of asteroid 4179 Toutatis with 6 cm waves. *Radiotekhnika Elektronika*, *38*, 1842–1850 (in Russian). Translation: Zaitsev A. L., Sokol'skiy A. G., Rzhiga O. R., Vyshlov A. S., Krivtsov A. P., and Shubin V. A. (1993) Radar investigations of the asteroid 4179 Tautatis at wavelength of 6 cm. *J. Comm. Tech. Electronics*, *38:16*, 135–143 (in English, by Scripta Technica, Inc., 1994).
- Zaitsev A. L., Ostro S. J., Ignatov S. P., Yeomans D. K., Petrenko A. G., Choate D., Margolin O. K., Cormier R. A., Mardyshev V. V., Winkler R., Rzhiga O. N., Jurgens R. F., Shubin V. A., Giorgini J. D., Krivtsov A. P., Rosema K. D., Koluka Y. F., Slade M. A., Gavrik A. L., Andreev V. B., Ivanov D. V., Peshin P. S., Koyama Y., Yoshikawa M., Nakamura A. (1997) Intercontinental bistatic radar observations of 6489 Golevka (1991 JX). *Planet. Space Sci.*, *45*, 771–778.